MULTI-SCALE ANALYSIS OF FIBRE REINFORCED STRUCTURES

B. Kurnatowski[1], M. Chatiri[2], A. Matzenmiller[1]

[1] *Universität Kassel, Institute für Mechanik Mönchebergstrasse 7, D-34125, Kassel, Germany, post-structure@.uni-kassel.de*
[2] *CADFEM GmbH, Grafing b. Munich, Germany, mchatiri@cadfem.de*

Abstract

Multi-scale methods of microheterogeneous fibre reinforced plastic material are used for the analysis of thick laminated composite structures with hundreds of layers through the cross-section such as for high pressure vessels. The conventional approach with the layerwise discretization of the laminate is often impractical, especially for non-linear step-by-step analysis due to inelastic behavior and transient effects. The overall behavior of thick multi-layered fiber-reinforced composite structures is accurately predicted by micro-mechanical homogenization at the fibre-matrix level and meso-mechanical homogenization at the laminate level. The meso-level laminate analysis is based on the 3D failure criteria of Puck and anisotropic continuum damage mechanics. Both approaches are in good agreement with each other as well as with experimental results.

1. Introduction

Structural analysis inevitably requires constitutive models linking the kinematic and equilibrium equations mathematically. Though, it is not always obvious how to describe a specific constitutive behavior by phenomenological models appropriately. This holds true particularly in the case of anisotropic composite materials which show load dependent anisotropic damage evolution with different modes of failure. Multi- or two-scale approaches mean a useful tool for characterizing the effective constitutive behavior of micro-heterogeneous materials from the solution of microscale boundary value problems. The anisotropic constitutive behavior at the larger scale results from the interactions of the small scale components. Micromechanical models, as used here, base on the concept of the statistically representative volume element (RVE), which can be regarded as a sample of the microstructure found by zooming in at the vicinity of a large scale material point $\mathcal{M}$, see Fig. 1. The practical application of multi-scale approaches requires numerical methods for discretizing and analyzing boundary value problems (BVP) on each scale under consideration.

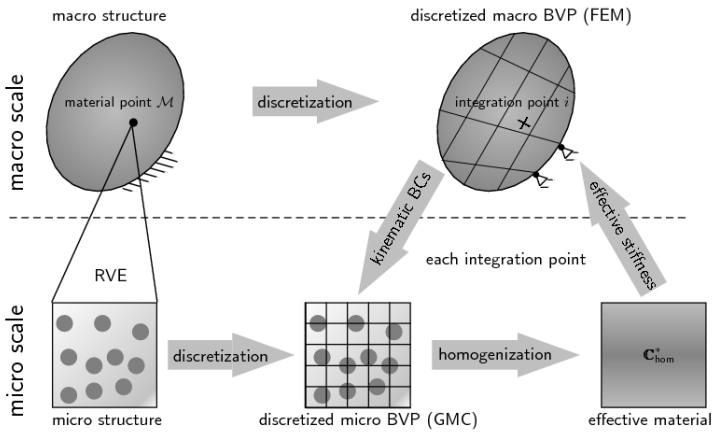

Figure 1. Schematic sketch of two scale analysis

The macroscopic structural level is discretized by the finite element method in this work. Since the constitutive equations are needed at every integration point of the macro structural finite element discretization, the maximum number of discrete microscale models to be solved is equal to the total number of integration points of the macro model. Hence, high numerical efficiency of micro modeling is essential. For this reason, the reformulated Generalized Method of Cells (GMC) is applied here, [1]. The original strain based version of the GMC by [2] has the potential of a numerically much more efficient reformulation without loss of accuracy. For higher resolutions of the microscale stress fields, the High Fidelity Generalized Method of Cells (HFGMC) was developed, see [3] and [4]. Though, the improved resolution of stresses by the HFGMC decreases the numerical efficiency. Applying the GMC seems a reasonable compromise between the conflicting targets of fidelity and efficiency. The information from the macro- to the microscale is transferred by prescribing the microscopic displacement boundary conditions (BCs) dependent on the macroscopic strain tensor $\boldsymbol{\epsilon}_i^{\mathrm{M}}$at the integration point i. Alternatively, stress boundary conditions might be formulated in terms of the macro-stress tensor. In the reverse direction, large scale variables $\mathbf{f}^{\mathrm{M}}$ (scalars, vectors or tensors) are commonly defined as the volume average $\langle \mathbf{f} \rangle$ of the corresponding small scale field $\mathbf{f}^{\mathrm{M}}(\mathbf{x})$:

$$\mathbf{f}^{\mathrm{M}} := \langle \mathbf{f} \rangle = \frac{1}{|V_{RVE}|} \int_{V_{RVE}} \mathbf{f}^{\mathrm{m}}(\mathbf{x}) \mathrm{d}V, \quad \mathbf{x} \in \mathcal{D}(V) \tag{1-1}$$

with $|V_{RVE}|$ as the content of the volume of the RVE, $\mathbf{x}$ as the position vector of a material point, and $\mathcal{D}$ as the domain of the RVE. It is emphasized that definition (1-1) holds for the macroscopic strain only in the case of a continuous displacement field $\mathbf{u}^{\mathrm{m}}$. Otherwise, the macro-strain is obtained as:

$$\boldsymbol{\epsilon}^{\mathrm{M}} = \langle \boldsymbol{\epsilon} \rangle - \frac{1}{2|V_{RVE}|} \int_{\Gamma_i} (\llbracket \mathbf{u} \rrbracket \otimes \mathbf{n} + \mathbf{n} \otimes \llbracket \mathbf{u} \rrbracket) \, \mathrm{d}A \tag{1-2}$$

with internal surfaces $\Gamma_{\mathrm{i}} = \partial\Omega_1 \cap \partial\Omega_2$ (normal $\mathbf{n} = \mathbf{n}^{[1]}$with respect to phase Ω_1) and displacement jumps $\llbracket \mathbf{u} \rrbracket = \mathbf{u}|_{\partial\Omega_1} - \mathbf{u}|_{\partial\Omega_1}$, see Fig. 2 and [5]. The homogenized effective constitutive tensor, $\mathbb{C}^*_{\mathrm{hom}}$, on the large scale is defined as:

$$\mathbb{C}^*_{\mathrm{hom}} := \frac{1}{|V_{RVE}|} \int_{V_{RVE}} \frac{\partial \boldsymbol{\sigma}^{\mathrm{m}}(\mathbf{x})}{\partial \boldsymbol{\epsilon}^{\mathrm{M}}} \, \mathrm{d}V \tag{1-3}$$

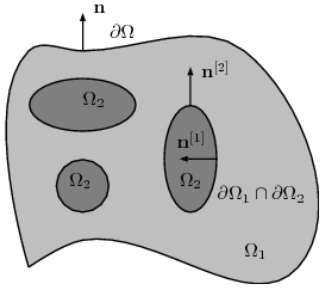

Figure 2. RVE with phases Ω_1, inclusions of phase Ω_2, and internal material interfaces Γ_{i}

2. Micromechanical analysis with the Generalized Method of Cells

The Generalized Method of Cells (GMC) is based on the concept of the representative volume element which is a statistically representative patch of the heterogeneous medium. It transforms the mechanical quantities $\mathbf{f}^{\mathrm{m}}$ from the micro to the macro level $\mathbf{f}^{\mathrm{M}}$ by averaging the variables over the volume V_{RVE} of the RVE, see (1-1). In the case of a nonlinear behavior of the bonding or the nascency and evolution of cracks, the average phase strain $\langle \boldsymbol{\epsilon}^{(i)} \rangle$ of the material phase (i) is a nonlinear process dependent tensor functional $\boldsymbol{\mathcal{A}}^{(i)}$ of the macroscopic strain tensor $\langle \boldsymbol{\epsilon} \rangle$ from the beginning at $\tau = 0$ up to time t.

$$\langle\boldsymbol{\epsilon}^{(i)}(t)\rangle := \boldsymbol{\mathcal{A}}^{(i)}\,[\langle\boldsymbol{\epsilon}(\tau)\rangle]_{\tau\geq 0}^{\tau=t} \;\rightarrow\; \dot{\boldsymbol{\epsilon}}^{(i)} := \frac{\mathrm{d}}{\mathrm{dt}}\langle\boldsymbol{\epsilon}^{(i)}\rangle = \frac{\mathrm{d}}{\mathrm{dt}}\boldsymbol{\mathcal{A}}^{(i)} = \frac{\partial\boldsymbol{\mathcal{A}}^{(i)}}{\partial\langle\boldsymbol{\epsilon}\rangle}\,\frac{\mathrm{d}\langle\boldsymbol{\epsilon}\rangle}{\mathrm{dt}} := \widetilde{\mathbb{A}}^{(i)}\colon\langle\dot{\boldsymbol{\epsilon}}\rangle \qquad (2\text{-}1)$$

The computation of its rate in eq. (2-1) leads to the tangential strain concentration tensor $\widetilde{\mathbb{A}}^{(i)}$ - see [6] and [7] as defined above. With the help of eq. (2-1), the rate of the average phase stress tensor $\langle\boldsymbol{\sigma}^{(i)}\rangle$ is computed:

$$\langle\dot{\boldsymbol{\sigma}}^{(i)}(t)\rangle := \frac{\mathrm{d}\langle\boldsymbol{\sigma}^{(i)}(t)\rangle}{\mathrm{dt}} = \frac{\partial\langle\boldsymbol{\sigma}^{(i)}(t)\rangle}{\partial\langle\boldsymbol{\epsilon}^{(i)}(t)\rangle}\,\frac{\mathrm{d}\langle\boldsymbol{\epsilon}^{(i)}\rangle}{\mathrm{dt}} = \frac{\partial\langle\boldsymbol{\sigma}^{(i)}(t)\rangle}{\partial\langle\boldsymbol{\epsilon}^{(i)}(t)\rangle} : \widetilde{\mathbb{A}}^{(i)}\colon\langle\dot{\boldsymbol{\epsilon}}\rangle \qquad (2\text{-}2)$$

Since N different phases $(i)-$ with volume fraction $c^{(i)} = \frac{|V^{(i)}|}{|V_{RVE}|}$ – are considered, the rate of the average macro stress tensor is computed from the rate of the macroscopic strain by means of the tangential strain concentration tensor $\widetilde{\mathbb{A}}^{(i)}$, the change of the phase stress tensor with respect to the phase strains and the volume fractions:

$$\langle\dot{\boldsymbol{\sigma}}\rangle = \sum_{i=1}^{N} c^{(i)}\frac{\partial\langle\boldsymbol{\sigma}^{(i)}\rangle}{\partial\langle\boldsymbol{\epsilon}^{(i)}\rangle} : \widetilde{\mathbb{A}}^{(i)}\colon\langle\dot{\boldsymbol{\epsilon}}\rangle \;\rightarrow\; \tilde{\mathbb{C}}^{*} := \sum_{i=1}^{N} c^{(i)}\frac{\partial\langle\boldsymbol{\sigma}^{(i)}\rangle}{\partial\langle\boldsymbol{\epsilon}^{(i)}\rangle} : \widetilde{\mathbb{A}}^{(i)} \;\rightarrow\; \langle\dot{\boldsymbol{\sigma}}\rangle = \tilde{\mathbb{C}}^{*}\colon\langle\dot{\boldsymbol{\epsilon}}\rangle \qquad (2\text{-}3)$$

The fibres behave linearly elastic. Since epoxy matrices show significantly nonlinear elastic response to shear loading, the matrix phase is modeled with a Ramberg-Osgood type of material equation $\epsilon_{ij} = \left[\frac{1+\upsilon}{E} + \Gamma\left(1-\delta_{ij}\right)\left(\frac{\sigma_{ij}}{\sigma_0}\right)^{(n-1)}\right]\sigma_{ij} - \frac{\upsilon}{E}\sigma_{kk}\,\delta_{ij}$ with Young's modulus E, shear modulus G, Poisson's ratio υ, and shear parameter Γ. The exponent n determines the degree of non-linearity. The GMC approach discretises the RVE by subdividing the displacement field $\mathbf{u}(\mathbf{x})$ which is then piecewisely approximated by linear functions defined on each subcell. The continuity of tractions is ensured along all subcell interfaces Γ_{sub}. Displacement discontinuities $[\![\mathbf{u}(\mathbf{x})]\!] = \mathbf{u}(\mathbf{x}^{+}) - \mathbf{u}(\mathbf{x}^{-})$, $\mathbf{x} \in \Gamma_{\mathrm{sub}} = \Gamma_{\mathrm{FM}} \cup \Gamma_{\mathrm{MM}}$ are conceded to arise at the common boundaries Γ_{FM} of neighbouring fibre and matrix subcells in order to model the imperfect bond of the phases. Predefined subcell interfaces Γ_{MM} of adjacent matrix cells serve also as localization nuclei for the initiation and growth of crack surfaces within the matrix phase. The interface traction vector $\mathbf{t} = \boldsymbol{\sigma}\mathbf{e}_n$ on the interboundaries of the subcells with the normal $\mathbf{e}_n$ is related to its kinematical counterpart, i.e. the separation vector $[\![\mathbf{u}]\!]$, via the traction-separation model given by [8]. This model involves two scalar valued stress and separation measures, both defined over past time $\tau \leq t$:

$$t_v(\tau) = \sqrt{\left(\frac{\langle t_n(\tau)\rangle}{R_{\perp}}\right)^2 + \left(\frac{t_t(\tau)}{R_{\parallel}}\right)^2 + \left(\frac{t_b(\tau)}{R_{\parallel}}\right)^2}, \quad \|\mathbf{u}(\tau)\| = \sqrt{\left(\frac{\langle[\![u_n(\tau)]\!]\rangle}{u_{\perp}}\right)^2 + \left(\frac{[\![u_t(\tau)]\!]}{u_{\parallel}}\right)^2 + \left(\frac{[\![u_b(\tau)]\!]}{u_{\parallel}}\right)^2} \qquad (2\text{-}4)$$

with the norm $\|\ \ \|$ of the vector components $(\ \ )_n, (\ \ )_t$, and $(\ \ )_b$ in normal, tangential, and bi-normal direction of the fibre. Herein, the normal and shear strengths are denoted by $R_{\perp}$and $R_{\parallel}$ respectively, whereas the characteristic length parameters $u_{\perp}$ and $u_{\parallel}$ determine the ductility in the traction-separation-model. As long as $\max_{\tau\leq t} t_v(\tau) < 1$ holds, neither elastic compliance nor damage of the bond between the subcells occurs, i.e. the bond flexibility and $[\![\mathbf{u}]\!]$ are zero, otherwise the traction vector $\mathbf{t}$ becomes a nonlinear vector-functional $\boldsymbol{\mathcal{F}}([\![\mathbf{u}]\!], q)$ of the current jump vector and the process dependant internal variable $q(t) := \min\{\max\|\mathbf{u}(\tau)\|_{\tau=0}^{\tau=t}, 1\}$:

$$\mathbf{t} = \boldsymbol{\mathcal{F}}[[\![\mathbf{u}(\mathbf{x})]\!], q] = \frac{1-3q^2+2q^3}{q}\left(\frac{R_{\perp}}{u_{\perp}}[\![u_n]\!]\mathbf{e}_n + \frac{R_{\parallel}}{u_{\parallel}}[\![u_t]\!]\mathbf{e}_t + \frac{R_{\parallel}}{u_{\parallel}}[\![u_b]\!]\mathbf{e}_b\right), \; [\![u_n]\!] > 0 \qquad (2\text{-}5)$$

The penetration of phases is numerically suppressed by setting $t_n = K_p[\![u_n]\!]$ with the penalty stiffness K_p. The continuity conditions, imposed on the microfields of stresses and displacements at the subcell boundaries [2] together with the constitutive equations of the interface model, lead to a system of nonlinear algebraic equations. Their solution finally provides the tangential strain concentration tensors $\widetilde{\mathbb{A}}^{(i)}$ for all subcell domains (i), see [9]. Hence, the macroscopic stress tensor $\langle\boldsymbol{\sigma}\rangle$ can be computed by numerical time integration of equation $(2\text{-}3)_3$ from the effective constitutive tensor $\tilde{\mathbb{C}}^{*}$ according to eq. $(2\text{-}3)_2$ for the given macroscopic strain process $\langle\boldsymbol{\epsilon}(t)\rangle$.

3. Failure analysis of UD laminae based on the homogenous continuum

3A.Failure criteria

The development of physically based failure criteria for inter fibre failure (IFF) in long fibre-reinforced polymer composites has been the focus of research for many years [10]. The Puck IFF criteria are most promising for brittle, plastic unidirectional (UD) laminates - see Fig. 3. The UD ply behaves transversely isotropic in both cases, elasticity and failure. Puck assumes a Mohr–Coulomb type of failure criterion for loading transverse through the fiber direction. Failure is assumed to be caused by the normal and shear components acting on the action plane of stress $(\sigma_n, \tau_{n1}, \tau_{nt})$ - see Fig. 3. Positive normal stress on this plane promotes fracture while a negative one increases the material's shear strength, thus, impeding fracture. Puck's stress based failure criteria enable the computation of the material exposure $f_{E,IFF}(\vartheta)$ as a failure indicator.

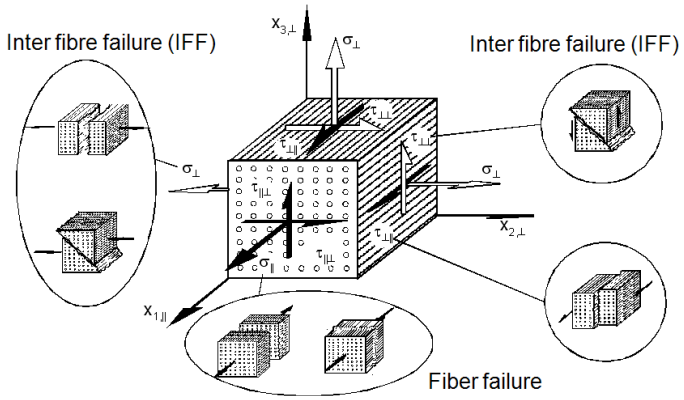

Figure 3. Schematic representation of failure modes and failure plane stresses taken from [10]

The values of $f_{E,IFF}(\vartheta)$ range between 0, where the material is unstressed, and up to 1, denoting the onset of IFF. The material exposure $f_{E,IFF}(\vartheta)$ is a function of the stress state $\boldsymbol{\sigma}$ and the orientation ϑ of the stress action plane against the thickness direction. The fracture plane stresses are obtained by rotating the three dimensional stress tensor from material coordinates to the fracture plane. The master failure surface on the fracture plane is defined in terms of Mohr-Coulomb stresses on the fracture plane, thus, yielding the following failure criteria [11]:

$$f_{E,IFF}(\vartheta) = \sqrt{\left[\frac{1}{R_{\perp}^{(+)}} - \frac{p_{\perp\psi}^{(+)}}{R_{\perp\psi}^{A}}\right]^2 \sigma_n^2 + \left[\frac{\tau_{nt}}{R_{\perp\perp}^{A}}\right]^2 + \left[\frac{\tau_{n1}}{R_{\perp\parallel}}\right]^2} + \frac{p_{\perp\psi}^{(+)}}{R_{\perp\psi}^{(A)}}\sigma_n \quad \text{for} \quad \sigma_n \geq 0 \tag{3-1}$$

$$f_{E,IFF}(\vartheta) = \sqrt{\left[\frac{\tau_{nt}}{R_{\perp\perp}^{A}}\right]^2 + \left[\frac{\tau_{n1}}{R_{\perp\parallel}}\right]^2 + \left[\frac{p_{\perp\psi}^{(-)}}{R_{\perp\psi}^{(A)}}\sigma_n\right]^2} + \frac{p_{\perp\psi}^{(-)}}{R_{\perp\psi}^{(A)}}\sigma_n \quad \text{for} \quad \sigma_n < 0 \tag{3-2}$$

The only unknown parameters in these equations are $p_{\perp\psi}^{(\pm)}$, $R_{\perp\psi}^{(A)}$, and $R_{\perp\perp}^{A}$ which can be expressed by the following equations :

$$\frac{p_{\perp\psi}^{(\pm)}}{R_{\perp\psi}^{(A)}} = \frac{p_{\perp\perp}^{(\pm)}}{R_{\perp\perp}^{(A)}} \frac{\tau_{nt}^2}{\tau_{nt}^2 + \tau_{n1}^2} + \frac{p_{\perp\parallel}^{(\pm)}}{R_{\perp\parallel}} \frac{\tau_{nt}^2}{\tau_{nt}^2 + \tau_{n1}^2}$$

$$R_{\perp\perp}^{A} = \frac{R_{\perp}^{(-)}}{2\left(1 + p_{\perp\perp}^{(-)}\right)}$$

wherein $R_{\perp}^{(+)}, R_{\perp\parallel}, R_{\perp}^{(-)}$ denote the material strength parameters, and $p_{\perp\perp}^{(\pm)}, p_{\perp\parallel}^{(\pm)}$ are Puck constants.

3B. Continuum damage model

The post-failure analysis is based on the plane stress continuum damage model in [12] which is extended into 3D stress space with additional modes of damage by introducing a third array of cracks orthogonal to the other two. This damage model characterizes the growth of damage by a decrease in the stiffness of the material. A set of damage variables ω_{i} is introduced to relate the onset and growth of damage to stiffness losses in the material. The compliance matrix **S** for the damaged material is:

$$\mathbf{S}=\mathbf{C}^{-1}=\begin{bmatrix} \frac{1}{(1-\omega_1)E_1} & -\frac{\nu_{21}}{E_2} & -\frac{\nu_{31}}{E_3} & 0 & 0 & 0 \\ -\frac{\nu_{12}}{E_1} & \frac{1}{(1-\omega_2)E_2} & -\frac{\nu_{32}}{E_3} & 0 & 0 & 0 \\ -\frac{\nu_{13}}{E_1} & -\frac{\nu_{23}}{E_2} & \frac{1}{(1-\omega_3)E_3} & 0 & 0 & 0 \\ 0 & 0 & 0 & \frac{1}{(1-\omega_4)G_{12}} & 0 & 0 \\ 0 & 0 & 0 & 0 & \frac{1}{(1-\omega_5)G_{23}} & 0 \\ 0 & 0 & 0 & 0 & 0 & \frac{1}{(1-\omega_6)G_{31}} \end{bmatrix}. \tag{3-3}$$

As suggested in [12], the rate of the damage variables $\dot{\omega}_i$, assembled in the vector $\dot{\boldsymbol{\omega}}$, are governed by the damage rule in the form of $\dot{\boldsymbol{\omega}} = \sum_{i=1}^{\mathrm{n\,modes}} \phi_i \, \mathbf{q}_i$, where ϕ_i controls the amount of growth and $\mathbf{q}_i$ provides coupling between the individual damage modes. In the present model, the three different failure modes, denoted as fiber mode, perpendicular and parallel matrix modes, are expressed by vectors $\mathbf{q}_i$ and *i*=1, .., 3**.** They couple the damage variables according to :

$$[\mathbf{q}_i]=\begin{bmatrix} 1 & 0 & 0 \\ 0 & 1 & 0 \\ 0 & 0 & 1 \\ 1 & 1 & 0 \\ 0 & 0 & 1 \\ 1 & 1 & 1 \end{bmatrix} \tag{3-4}$$

In the softening range of post failure, the damage variables can be obtained in the form of $\omega = 1 - e^{\frac{1}{m}(1-[r]^m)}$, $r \geq 1$ where m is the strain softening parameter and r is the damage threshold. At the onset of failure, triggered by the criteria, the value of ω_{i} is zero. As the damage progresses, ω_{i} increases and, therefore, eventually diminishes the stiffness of the material until it reaches a final value of zero.

4. Numerical Examples

The Generalized Method of Cells is implemented as the constitutive model into the finite element code FEAP, see [13], and used with the enhanced 3D-solid displacement element as outlined in [14]. A multi-layered solid element with thickness homogenization at the laminate level is available in the code of [15], where the failure and damage model, based on the homogenous continuum, is implemented and further referred as meso-level approach. The fibre orientation can be defined for arbitrary angles with respect to the global co-ordinate system. The examples are computed by both, a coupled two scale analysis, as outlined in section 2, and a meso-level approach with the multi-layered solid element and compared below.

4A. Verification example: Thin-walled tube

The thin-walled, single-layered composite tube in Fig. 4 a) serves as a verification example for the coupled twoscale analysis and the meso-level approach with the multi-layered solid element. The inner and outer radii of the tube are $r_{\mathrm{i}} = 16.5$ mm and $r_{\mathrm{a}} = 18.5$ mm with a tube length of $l_{\mathrm{x}} = 100$ mm. The angle of the filament winding relative to the cylinder axis x_3 is denoted by θ. The composite

consists of the E-glass-fibre reinforced epoxy resin MY750 with a fibre volume content of $v_f = 60\%$. The strength values and stiffness parameters of the constitutive models, used to describe the mechanical behavior of the phases, are taken directly from the World-Wide Failure Exercise (WWFE) [16] pp 37 whereas the interface parameters are inversely identified with the help of the experimental data published as part of the WWFE – see [17]. Tab. 1 gives the elasticity parameters for the phase materials, as well as the parameters of the interface model according to Lissenden for the fibre-matrix-bond and matrix fracture. The strength parameters, Puck constants in the failure criteria in (3-1) or (3-2) and the elasticity moduli of the E-glass-fiber reinforced epoxy resin MY750 are taken from the WWFE [16], pp 36, as well as [11], pp 846 and added also to Table 1. The FE mesh consists of 36 elements in circumferential direction and one element through the thickness of the layer. The tube is discretized by 10 elements in axial direction. Along the boundary at $x_3 = 0$, degrees of freedom for u_3 and u_φ are suppressed where u_3 is the axial and u_φ the tangential displacement component. The load is applied in terms of prescribed displacements versus time up to the end value $u_3(\mathrm{l}) = 0.3$ mm at the far end of the tube along the edge at $x_3 = l$ in axial direction. The fibres run in circumferential direction ($\theta = 90^\circ$). Hence, the normal stress caused is perpendicular to the fibres.

Phase material	E[GPa]	G[GPa]	σ_0 [GPa]	n	Γ[GPa]
E-glass $v_f = 0.6\%$.	74	30.8	-	-	-
epoxy resin MY750	4.9	1.9	117.5	9	2.0
Interface model	$R_{\mathrm{I}\perp}$[MPa]	$R_{\mathrm{I}\parallel}$[MPa]	$u_{\mathrm{I}\perp}[\mu m]$	$u_{\mathrm{I}\parallel}[\mu m]$	-
fibre-matrix-bond	48	77	0.004	0.12	-
matrix fracture surfaces	15	60	0.004	0.12	-
UD composite strength parameters	$R_\perp^+$[MPa]	$R_{\perp\parallel}$[MPa]	$R_\perp^-$[MPa]	$R_\parallel^+$[MPa]	$R_\parallel^-$[MPa]
	40	73	145	1280	800
Puck constants	$p_{\perp\parallel}^{(+)}$	$p_{\perp\parallel}^{(-)}$	$p_{\perp\perp}^{(\pm)}$		
	0.25	0.3	0.13		
elasticity moduli	$E_\parallel$[GPa]	$E_\perp$[GPa]	$G_{\parallel\perp}$[GPa]	$\nu_{\parallel\perp}$	$\nu_{\perp\perp}$
	45.6	16.2	5.83[1]	0.278	0.4

Table 1. Parameters for E-glass, epoxy resin MY750, interface and composite

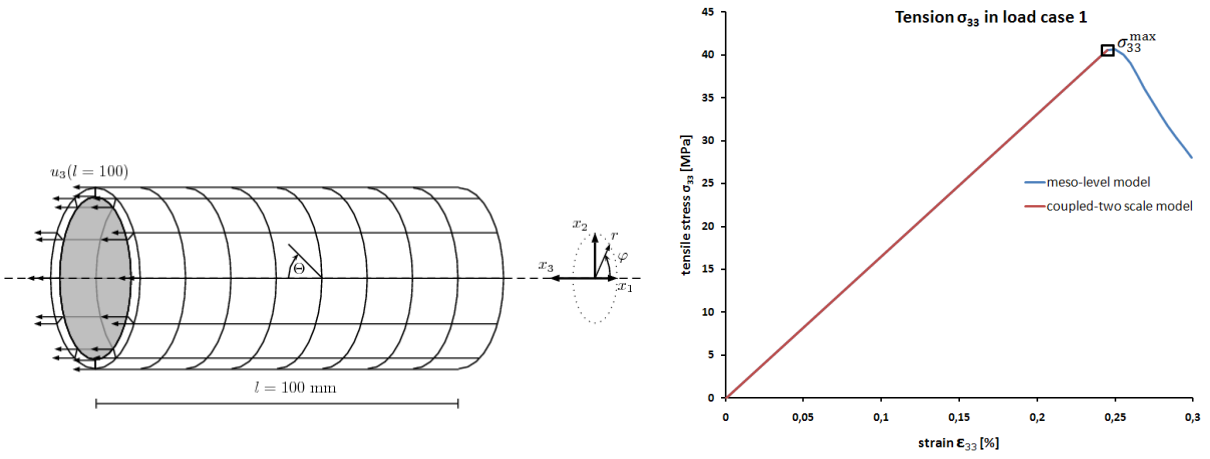

Figure 4. a) Geometry of thin-walled tube. b) Tension stress σ_{33} vs. strain ϵ_{33} in coupled-two scale analysis and meso-level approach

Fig. 4 b) depicts the tensile stress σ_{33} versus the strain $\epsilon_{33} = u_3(100)/l$ due to the prescribed displacement relative to the tube length $u_3(l)/l$. Up to failure at the stress level of $\sigma_{33}^{\max} = 40.5$ MPa in the coupled twoscale analysis or 40 MPa in the meso-level approach, the normalized load-displacement is linear. After reaching the strength limit, the stress-strain diagram deviates in the

[1] Nonlinear behavior and stress strain curves and data points are provided

coupled two-scale analysis from the meso-level approach. The stress curve gradually falls after failure. The results from both the methods match with the experimental data from WWFE [16].
In load case 2, a path-controlled torsional deflection is applied at the far end of the tube. The prescribed deformation causes a homogenous shear stress in the tube. Hence, the composite is exposed to an axial shear loading due to the fibre orientation. The load bearing capacity of the tube under torsional loading is reached for the shear stress at $\tau_{3\varphi} \approx 70$ MPa in both the approaches compared to an experimental axial shear strength value $R_{\perp\parallel}$ of 73 MPa. In load case 3, combined tension/shear stress loadings are applied and the computed fracture curves are compared to experimental results, which shall be explained in the talk.

4B. Validation example: Cross-ply laminate under uniaxial tensile loading
The cross-ply laminate with four UD layers $[0^\circ/90^\circ/90^\circ/0^\circ]$ in Fig. 5 is made of E-glass/MY750 epoxy resin with $v_f = 0.62$ and used to validate both approaches. The test specimen's length is $l_x = 200$ mm, the width $l_y = 25$ mm and the total thickness $l_z = 4 \times 0.475 = 1.9$ mm. The fibre direction in the outer layers coincides with the loading direction. The two-scale FE-model in Fig. 5 consists of three solid elements through the thickness, whereas the FE model for the meso-level approach uses one multi-layered 8-node (linear) solid (MLS) element with four integration points to take into account the various fibre orientations given above. The option of representing several plies in

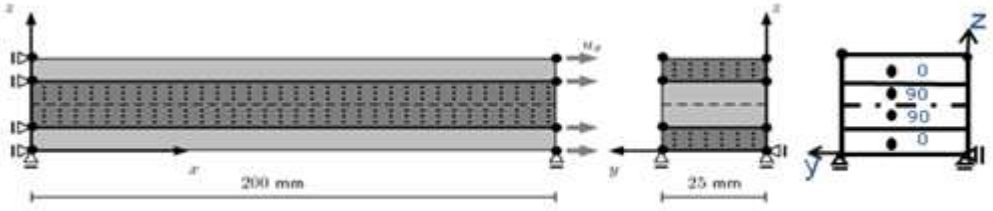

Figure 5. FE-model of cross-ply laminate: longitudinal view, cross section and fibre angles

one solid element and more such elements across the thickness is implemented into the code of [15]. Like any linear brick element, the MLS resolves the 3D stress state, but may contain n-layers from the composite laminate. It is assumed to be small in comparison to the overall size of the composite thickness. Its in-plane behavior is treated by through-the-thickness integration, whereas the transverse properties in the shear and normal mode for the hexahedron element must be based on the concept of a homogeneous substitute material, since the underintegrated linear element relies on a uniform membrane stress state. Hence, homogenization of the layer dependent properties is required through the thickness of the element. The homogenization result is bounded by Voigt's [18] and Reuss's [19] hypotheses. The Reuss bound for laminae, connected in series, is close to the effective elasticity modulus in transverse normal direction, whereas the Voigt bound for laminae, assembled in parallel, serves as an upper limit and approximates the transverse shear modulus of the laminate tightly. Both bounds are implemented into the code of [15] to compute the transverse stresses from the strains.

The boundary conditions, imposed on the nodal displacements do not constrain lateral extensions of the specimen. The simulation is controlled by the displacement u_x given at the right end with $l_x = 200$ mm. In Fig. 6, the average laminate stress σ_{xx} is plotted versus the average strain $\epsilon_{xx} = u_x/l_x$ as well as the lateral average strain $\epsilon_{yy} = u_y/l_y$ as founded by tests published in [20]. At the average longitudinal stress $\sigma_{xx} = 116$ MPa, first cracks perpendicular to the loading direction are observed experimentally in the embedded layer with fibres in 90°-direction, causing a slight reduction of the laminate's tensile stiffness, represented by the small kink in the stress-strain diagram. At $\sigma_{xx} = 325$ MPa, cracks occur parallel to the loading direction at the outer layers in the test, see [20]. The damage is due to the tensile stress σ_{yy} resulting from the lateral strain ϵ_{yy} which is obstructed by the large stiffness of the inner layers in loading direction. At $\sigma_{xx} = 600$ MPa, final failure of the laminate is provoked by tensile fibre fracture in the upper and lower layer.
The green curves in Fig. 6 (left) are computed with the two-scale analysis by using the UD parameters for the composite material as given in Tab. 1. Beyond the stress level of $\sigma_{xx} \approx 80$ MPa, the softening of the embedded layer causes a physically premature decrease of the computed laminate stiffness. It is

a matter of common knowledge that the constitutive behavior of a single UD-layer differs from that of the same layer being part of a laminate structure [21]. Experiments reveal that the embedded lamina withstands higher loading than the isolated one. Hence, underestimating the stiffness and strength of the laminate is not unexpected, if UD-parameters from a single laminae are used for the prediction of the overall behavior of a multilayer composite. Longitudinal cracks at the covering layers do appear in the simulation too early, here, at an average stress of $\sigma_{xx} \approx 300$ MPa and lead to the loss of convergence of the computation. Alternatively, if the matrix and the bond stress limits are set equal to the bulk strength of the resin, the blue stress-strain-curves in Fig. 6 are predicted for the mechanical response of the cross-ply laminate. Obviously, the influence of damage in the embedded layer on the decrease of the laminate stiffness is portrayed quite well. The final failure simulation of the composite, caused by fibre fracture in the outer layers, is not part of the micromodel at hand but might be easily incorporated into the cell's ansatz by defining additional fracture planes in the cross section of the fibres.

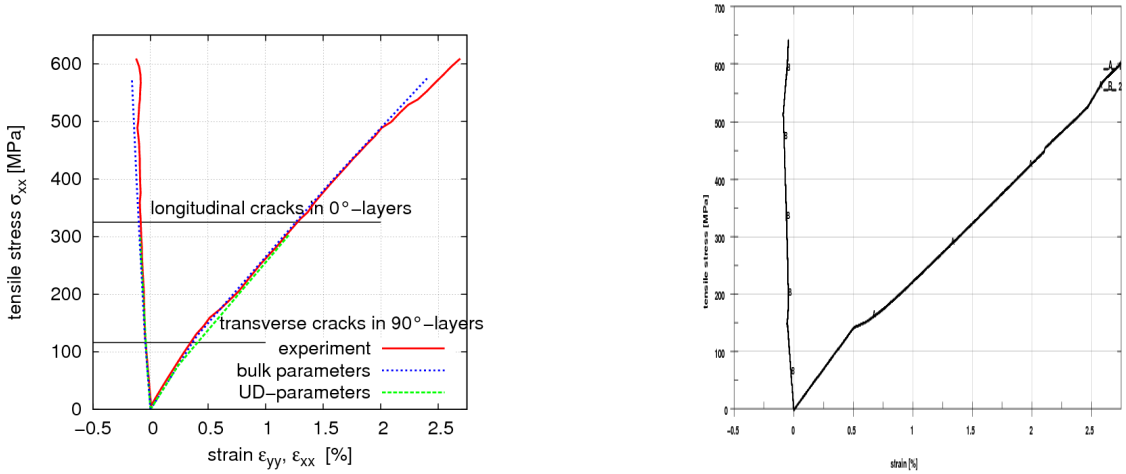

Figure 6. Average stress (σ_{xx}) vs. longitudinal (ϵ_{xx}) and transverse strain (ϵ_{yy}) in coupled-two scale analysis (left) and meso-level model (right) and compared to experimental results from [20]

In the meso-level model the first transverse cracks in the 90°-layers appear at the average stress level of $\sigma_{xx} \approx 120$ MPa and the longitudinal cracks in the 0°-layers appear at $\sigma_{xx} \approx 340$ MPa. At $\sigma_{xx} \approx 640$ MPa, final failure of the laminate is computed by tensile fibre fracture in the upper and lower layers.

5. Summary and concluding remarks

In this contribution the efficiently reformulated version of the Generalized Method of Cells is used as the constitutive model for unidirectionally reinforced composites in the context of multiscale methods. The meso-level model with the 3D Puck failure criteria and anisotropic continuum damage mechanics is very effective in analyzing thick multi-layered structures having a large number of plies. The numerical implementation of the coupled twoscale analysis and the meso-level approach has been verified by analysing a single-layered thin-walled tube under homogeneous tensile and shear stress loading. The cross-ply laminate under uniaxial tension is used as the first example for the validation for both approaches. Further validation has to be done with test data, taken from non-homogenous states of stress in multi-layered composites.

Acknowledgement

The second author gratefully acknowledges financial support and helpful discussions with Drs. Stephan Fell from GM Alternative Propulsion Center Europe, Ruesselsheim, Germany and Matthias Hoermann from CADFEM GmbH, Grafing, Germany.

References

[1] M. J. Pindera and B. A. Bednarcyk, "An efficient implementation of the generalized method of cells for unidirectional, multi-phased composites with complex microstructures," *Compos. Part B: Engineering*, no. 30, pp. 87-105, 1999.

[2] J. Aboudi, *Mechanics of Composite Materials. A Unified Micromechanical Approach.* Studies in Applied Mechanics 29: Elsevier, Amsterdam, 1991.

[3] J. Aboudi, "The Generalized Method of Cells and High-Fidelity Generalized Method of Cells micromechanical models – a review," *Mechanics of Advanced Materials and Structures*, no. 11, pp. 329-366, 2004.

[4] R. Haj-Ali and J. Aboudi, "Nonlinear micromechanical formulation of the high fidelity generalized method of cells," *J. Solids and Structures*, no. 46, pp. 2577–2592, 2009.

[5] P. Wriggers and T. Zhodi, "Introduction to Computational Micromechanics," in *Lecture Notes in Applied and Computational Mechanics*. Vol 20, Springer-Verlag: Berlin, Heidelberg, 2005.

[6] R. Hill, "Elastic properties of reinforced solids: some theoretical principles," *J. Mech. Phys. Solids*, no. 11, pp. 357-372, 1963.

[7] B. Koester and A. Matzenmiller, "Two-scale simulation of damage in unidirectionally fibre reinforced composite materials," *Appl. Math. Mech*, Vol. 7, pp. 4080025-4080026, 2007.

[8] C. J. Lissenden, "An approximate representation of fibre-matrix debonding in nonperiodic metal matrix composites," *Damage and Interfacial Debonding in Composites*, pp. 189-212, 1996.

[9] A. Matzenmiller and B. Koester, "Consistently linearized constitutive equations of micromechanical models for fibre composites with evolving damage," *Int. J. Solids and Structures*, no. 44, pp. 2244–2268, 2007.

[10] M. Knops, *Analysis of Failure in Fiber Polymer Laminates: The Theory of Alfred Puck.* Springer-Verlag: Berlin, Heidelberg, 2008.

[11] A. Puck and H. Schürmann, "Failure analysis of FRP laminates by means of physically based phenomenological models," in *Failure Criteria in Fibre Reinforced Polymer Composites: The World-Wide Failure Exercise*, P. D. Hinton, A. S. Kaddour, and M. L. Soden, Eds. Elsevier: Oxford, pp. 832-876, 2004.

[12] A. Matzenmiller, J. Lubliner, and R. L. Taylor, "A constitutive model for anisotropic damage in fiber composites," *Mechanics of Materials*, no. 20, pp. 125-152, 1995.

[13] R. L. Taylor and O. C. Zienkiewicz, *The Finite Element Method*: McGRAW-HILL Book Company Europe, 1989.

[14] M. Fiolka and A. Matzenmiller, "On the resolution of transverse stresses in solid-shells with a multi-layer formulation," *Commun. Numer. Meth. Engg.*, no. 23, pp. 313-326, 2007.

[15] J. O. Hallquist, *LS-DYNA Theoretical Manual*. Livermore: Livermore Software Technology Corporation, 2010.

[16] P. D. Soden, M. J. Hinton, and A. S. Kaddour, "Lamina properties, lay-up configurations and loading conditions for a range of fibre reinforced composite laminates," in *Failure Criteria in Fibre Reinforced Polymer Composites: The World-Wide Failure Exercise*, P. D. Hinton, A. S. Kaddour, and M. L. Soden, Eds. Elsevier: Oxford, pp. 30-51, 2004.

[17] B. Kurnatowski, "Zweiskalensimulation von mikroheterogenen Strukturen aus spröden Faserverbund-werkstoffen," Institut für Mechanik, Fachbereich Maschinenbau, Universität Kassel, Ph. D. Thesis, 2010.

[18] W. Voigt, "Über die Beziehung zwischen den beiden Elastizitätskonstanten isotroper Körper," *Wied. Ann*, no. 38, pp. 573-587, 1889.

[19] A. Reuss, "Berechnung der Fließgrenze von Mischkristallen auf Grund der Plastizitätsbedingung für Einkristalle," *Z. Angew. Math. Mech*, no. 9, pp. 49-58, 1929.

[20] P. K. Gotsis, C. C. Chamis, and L. Minnetyan, "Application of progressive fracture analysis for predicting failure envelopes and stress-strain behaviors of composite laminates: a comparison with experimental results," in *Failure Criteria in Fibre Reinforced Polymer Composites: The World-Wide Failure Exercise*, P. D. Hinton, A. S. Kaddour, and M. L. Soden, Eds. Elsevier: Oxford, pp. 703-723, 2004.

[21] R. G. Cuntze, "Efficient 3D and 2D failure conditions for UD laminae and their application within the verification of the laminate design," *Composites Science and Technology*, no. 66, pp. 1081-1096, 2006.